Composite Structures 348 (2024) 118502

Contents lists available at ScienceDirect

Composite Structures

journal homepage: www.elsevier.com/locate/compstruct

Experimental and performance validation of a full-scale morphing droop nose design based on composite compliant structures

Alessandro De Gaspari [*,1], Vittorio Cavalieri[2], Sergio Ricci[3]

Department of Aerospace Science and Technology, Politecnico di Milano, Via La Masa 34, 20156 Milano, Italy

ARTICLE INFO

Keywords:
Design optimization
Aerospace applications
Composite compliant structures
Experimental testing
Morphing wing

ABSTRACT

Active camber morphing technology can be used to improve aircraft performance in takeoff and landing flight conditions, while preserving a smooth wing shape. This study begins with the design of a morphing droop nose to be installed on a regional aircraft, and focuses on the manufacturing and testing of a full-scale and fully representative experimental prototype. All work is driven by the morphing shape change, which was optimized to provide the required aerodynamic performance. The adoption of a composite structure that combines a flexible skin with a compliant structure makes this device capable of achieving such a shape change, and sufficiently insensitive to external load variations. These capabilities are successfully demonstrated through experimental testing. A validation phase was conducted based on strain gauge measurements, and a motion capture system was used to identify three-dimensional shape changes due to the morphing. Finally, a validated numerical model is used to assess the aerodynamic performance of the experimental prototype.

1. Introduction

Adaptive wing technology exploits structural deformation to optimize the shape of lifting surfaces in all phases of aircraft flight. It distinguishes between fully adaptive wings and active camber wings by the ability of the structural wing box to take part in the morphing process. Multi-stable composite structures are a recent but promising opportunity for the twisting control of fully adaptive composite wings [1], as well as there is some attempt to involve the wing box in the induced deformation through the use of compliant cellular structures based on the design of chiral honeycomb cores [2,3]. On the other hand, most active camber wings consist of morphing devices installed around a traditional wing box, with greater level of technological maturity achieved today. They usually are composite structures able to actively or passively provide some kind of morphing deflection. In the case of trailing edge devices, bistable composite laminates can be used in various morphing applications, as they involve low energy actuation systems and high fatigue life [4]. Otherwise, corrugated structures can be used to manufacture the internal core of adaptive trailing edges [5] or to exploit the anisotropy of corrugated panels [6] in combination with other morphing concepts, such as the Fishbone active camber [7].

Focusing on leading edge devices, various solutions based on a flexible skin coupled with an internal mechanism composed of a cascade of rigid levers and kinematic joints have been proposed over the years. One of the pioneering activities dates back to the mission adaptive wing (MAW) program that equipped an F-111 A test bed research airplane with a smooth variable-camber mission adaptive wing. The design incorporated flexible fiberglass skins on the upper leading and trailing edges, while the bottom skin was cut to obtain a discontinuity that allows for overlapping sliding panels [8].

More recent activities have focused on the development of morphing droop nose devices for use in high lift conditions, based on a fully compliant skin fixed to both the upper and lower spar caps to avoid any type of discontinuity. Interesting solutions capable of obtaining very high deflection angles have been proposed by DLR over the years [9,10]. The thin composite skin concept proposed by DLR in [11] was further developed through the optimization of a variable stiffness skin to improve the quality of external deformation, after freezing the topology of the internal mechanism [12]. Compared to the sliding skin solution, these smooth and gap-less solutions are more promising from an aerodynamic point of view, but require higher actuation forces to deform the skin. For this reason, within the EU funded SARISTU project, Airbus developed a kinematic solution dedicated to the actuation of an unslotted adaptive droop nose prototype, showing significant benefits in terms of reduction in weight and required actuation force [13].

* Corresponding author.
E-mail address: alessandro.degaspari@polimi.it (A. De Gaspari).
[1] Associate Professor.
[2] PostDoctoral Researcher.
[3] Full Professor.

https://doi.org/10.1016/j.compstruct.2024.118502
Received 24 April 2024; Received in revised form 23 July 2024; Accepted 16 August 2024
Available online 17 August 2024

However, solutions based on rigid mechanisms suffer from the typical issues of mechanical components, such as wear, backlash, total weight, friction, and the disadvantages associated with numerous assembled parts. In addition, mechanical hinges transmit forces from the internal mechanism to the external skin, but are not able to transmit moments, so that once the device is activated, non-optimal aerodynamic shapes are obtained. Then, the friction in the joints further increases the actuation force and the backlash between different mechanical parts makes the shape achievable during flight uncertain [14].

Moreover, although the purpose of these devices is to generate high lift coefficients, delaying stall and providing smooth and gap-less skin deformation, the works cited above almost never refer to aerodynamic performance. Such morphing concepts are designed without starting from the aerodynamic requirements and, except in a few cases [15], the aerodynamic performance is not even verified a posteriori. The aerodynamic performance is closely linked to the shape quality of the deformed skin, but even this type of assessment, carried out under different loading conditions, is often overlooked.

This article proposes the experimental and performance verification of a morphing droop nose device, designed through a multi-disciplinary and multi-level optimization method that starts from the required aerodynamic performance and exploits the concept of composite compliant structure. This structural concept is based on the distributed compliance concept, originally proposed in [16], and extended in this work to the design of a composite structure consisting of an effective combination of parts made of aluminum alloy and parts made of glass fiber fabric. Compliant structures represent an alternative to the rigid kinematics. They spread the elastic deformation inside the entire structure, thus reducing stress concentrations and overcoming the typical mechanical component issues mentioned above. In this way, the load-carrying capability typical of structures is conciliated with the ability to transmit forces typical of mechanisms, reducing the overall weight. Applying this concept to the design of morphing devices gives them the flexibility needed to change shape by deforming, and the stiffness for maintaining insensitive to the aerodynamic loads. Indeed, devices installed on a variable camber wing must behave like control surfaces, so the shape variation that they introduce into the wing must be deterministic and not dependent on external load variations [17].

In the first section of this article the design optimization phases that led to the development of the presented morphing droop nose device are summarized. All other sections focus on the manufacturing, experimental testing and validation of a full-scale prototype derived from the previous design. The aim of this study is to carry out functionality tests, evaluate the quality of the achievable morphed shapes and validate the expected performance of the prototype. Experimental activities constitute a key step for two main reasons. The potential benefits of morphing, estimated through numerical simulations, are often in conflict with the technological aspects related to the implementation on real aircraft. Testing the full-scale prototype therefore represents an opportunity at the end of the design process to address manufacturing and installation issues. The results of the laboratory tests also allow the validation of a structural numerical model which is used to assess the aerodynamic performance of the prototype and its ability to deform while being insensitive to external loads applied to the skin.

2. Design optimization of the morphing droop nose

The morphing droop nose developed in this study is one of the technologies to be installed on the innovative wing of a turboprop Regional Aircraft (RA), within the framework of the Clean Sky 2 REG-IADP Airgreen 2 project [18]. The main goal of this device is to delay the wing stall in high-lift conditions, preserving the Natural Laminar Flow (NLF) wing shape in cruise. The structural flexibility allows the device to deflect, modifying its shape, without introducing geometric discontinuities and avoiding any kind of step and gap over the skin. The maximum achievable deflection depends on the skin structural

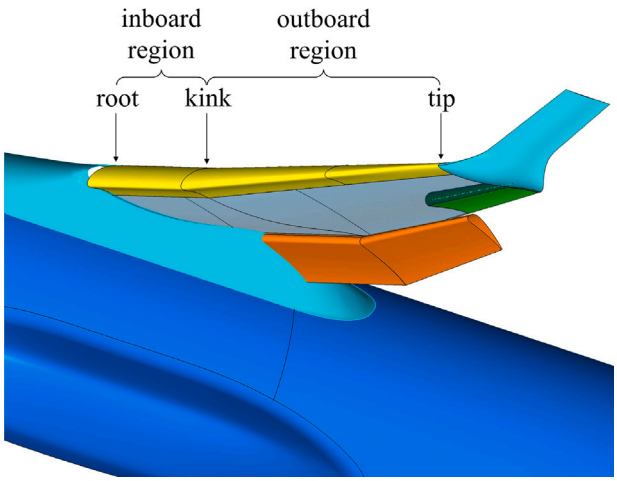

Fig. 1. Wing configuration and target shape of morphing droop nose.

constraints, according to the material properties and position of the front spar which is placed at 16% of the local chord. The complete configuration of the morphing droop nose is depicted in Fig. 1. The droop nose device covers both the inboard and outboard wing regions, the former extending from the wing root to the wing kink, the latter starting from the kink. In the outboard region, the active device starts at the kink and ends after 5.2 m along the span, where the deflection begins to linearly decrease until vanishing at the wing tip.

The design of the morphing droop nose was based on a multi-level and multi-disciplinary optimization consisting of four main steps [17,19]. The complete design optimization procedure is represented in Fig. 2. Starting from the design requirements, an aero-structural shape optimization first defined the morphing's optimal external shape able to guarantee the required aerodynamic performances. The obtained shape was used as target shape for the subsequent structural design phase: a topology optimization designed the droop nose compliant structure, including the skin, able to bear external loads and to deform itself for matching, once actuated, the target shape. Then, the structural design was refined and finalized through a sizing optimization. In the last step, high-fidelity models were used to perform virtual functionality tests on the complete device installed on the wing-box.

2.1. Aero-structural shape optimization

The aero-structural shape optimization is based on the Class-Shape function Transformation (CST) technique which is a geometry parameterization method that has been appropriately modified to introduce shape changes due to the morphing, taking into account the structural behavior of the skin [20]. This shape optimization was applied to the wing of the RA with the aim of maximizing the droop nose deflection and, at the same time, reducing the aerodynamic drag coefficient in high-lift conditions. The optimization scheme consists of two nested optimization loops: the inner one produces only feasible morphing shapes, while the outer one performs the aerodynamic evaluations. In this way, only morphing shapes that meet the structural requirements of the morphing skin are considered during the aerodynamic computation. The aerodynamic performances were evaluated at the aircraft level, in combination with the morphing flap developed by the Federico II University [21], by means of computational fluid dynamics (CFD) computations using the ONERA elsA software [22]. Two structural constraints were embedded in the droop nose design scheme: the skin length computed in the airfoil section was constrained to be constant during the optimization process, according to the constant cross-section length (CCL) strategy [23]; the bending strain was limited below 1%

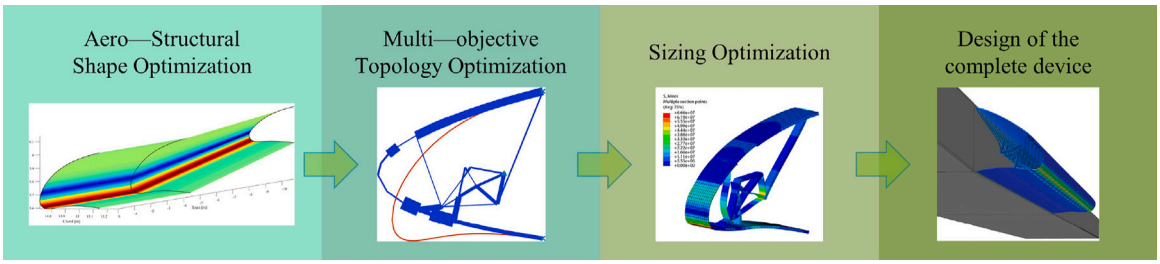

Fig. 2. Multi-level design optimization.

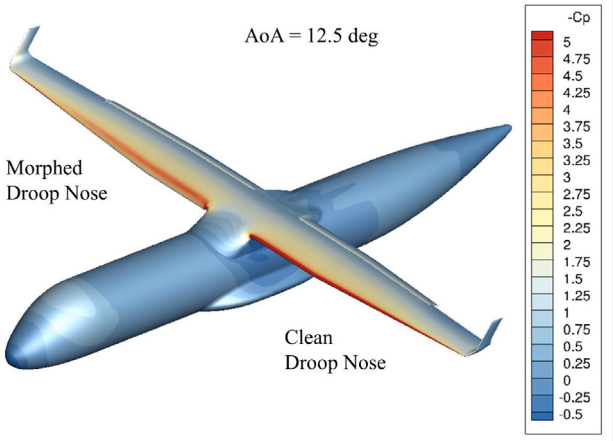

Fig. 3. Comparison between the wing pressure distribution with undeflected droop nose (left half wing) and with morphing droop nose at maximum deflection (right half wing) at 12.5 deg angle of attack.

which corresponds to a maximum skin curvature change of 20 m^{-1}, according to a minimum skin thickness of 1 mm.

The described optimization finds the optimal shape depicted in Fig. 1. The maximum droop deflection is equal to 16.2 deg which is constant in the inboard region. In the outboard region, the deflection linearly decreases from 16 deg at the kink to 10 deg before the aileron. The pressure coefficient distribution over the wing with morphed droop nose, compared to the baseline wing, is depicted in Fig. 3. The use of the morphing droop nose increases the stall angle by 2.5 deg in the take-off configuration, which is more than required by the performance design requirements, and by 5 deg in the landing configuration, making the device necessary to achieve the design requirements. Indeed, at higher angles of attack, the droop nose device delays the stall onset and enables to achieve the design lift coefficient. It is found that the combined use of morphing droop nose and flap allows to meet the aerodynamic requirements in landing condition, which is not possible with the flap only [24].

2.2. Topology optimization

The optimal shape was then used as target shape for the design of the droop nose compliant structure. This phase involves the use of an in-house design tool consisting of a topology optimization, based on a load-path representation method [23] coupled with nonlinear finite element analyses and a dedicated multi-objective genetic algorithm (MOGA). The multi-objective approach enables the simultaneous satisfaction of the conflicting requirements characterizing morphing solutions. Two different types of objective functions were considered in this study to meet both kinematic and structural requirements. The structural requirement guaranteed the load-carrying capability of the structure, while preserving the NLF wing shape when the device was not actuated. This was implemented by minimizing the strain energy of the undeployed device, under the aerodynamic loads corresponding to the dive speed condition at sea level (Mach = 0.48). The kinematic requirement guaranteed the attainment of the morphing shape. This was implemented by minimizing the least-squared error (LSE) between the target shape and the skin deformation of the droop nose due to morphing, under the aerodynamic loads corresponding to the landing flight condition at sea level (Mach = 0.197 and 10 deg angle of attack). Moreover, the maximum normal strain within the internal structure, calculated as the combination of axial and bending strains, was minimized to assure structural feasibility. This optimization was conducted considering a limited spanwise extension of the device, corresponding to the distance between two compliant ribs. Isotropic materials with mechanical properties equivalent to the actual materials of the subsequent sizing optimization were adopted: glass fiber for the skin and aluminum alloy for the rib.

The outcome of the multi-objective optimization is a Pareto front, which was used to select the optimal solution as a satisfactory compromise between conflicting kinematic, structural and strain requirements, taking into account manufacturing requirements not included in the optimization problem [19]. The selected topology solution, representing the starting point for the next design phase, is depicted in Fig. 4 which explains how the device works.

2.3. Sizing optimization

This optimization level assumes the previously determined topology solution and only acts on sizing variables, taking into account actual materials and design aspects not included in the finite element models (FEMs) adopted by topology optimization. A model of the type represented in Fig. 4 was used for the design of several sections of the full-scale device along the wingspan. A single rib and a reduced spanwise extension of the skin, equal to 260 mm, were considered and constant material properties in the spanwise direction were assumed. In this final solution, the skin was made of glass fiber composite material and the internal compliant rib was made of glass fiber combined with aluminum alloy, exploiting the high elongation of the glass fiber material to meet material limits also in the most strained internal regions.

Two different algorithms were used to determine the optimal sizing variables according to the material choice, while the topology solution was kept fixed: a simpler MOGA than the one adopted by the topology optimization, considering the same objective functions; a single-objective sequential quadratic programming (SQP) algorithm, preserving only one of the previous objective functions and making the others constraint functions. Sizing variables included the thickness of each element belonging to the internal rib and the thicknesses associated with ten skin sectors which were appropriately defined to determine the optimal skin thickness distribution. In this phase, care was taken to verify that the device was able to satisfy both the structural and kinematic requirements without its deformation being affected by the magnitude of the external aerodynamic loads nor by the considered flight condition.

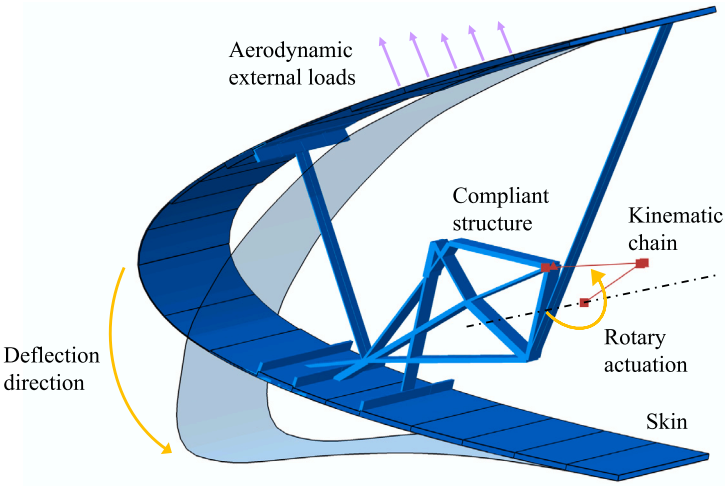

Fig. 4. Working principle of the compliant droop nose device.

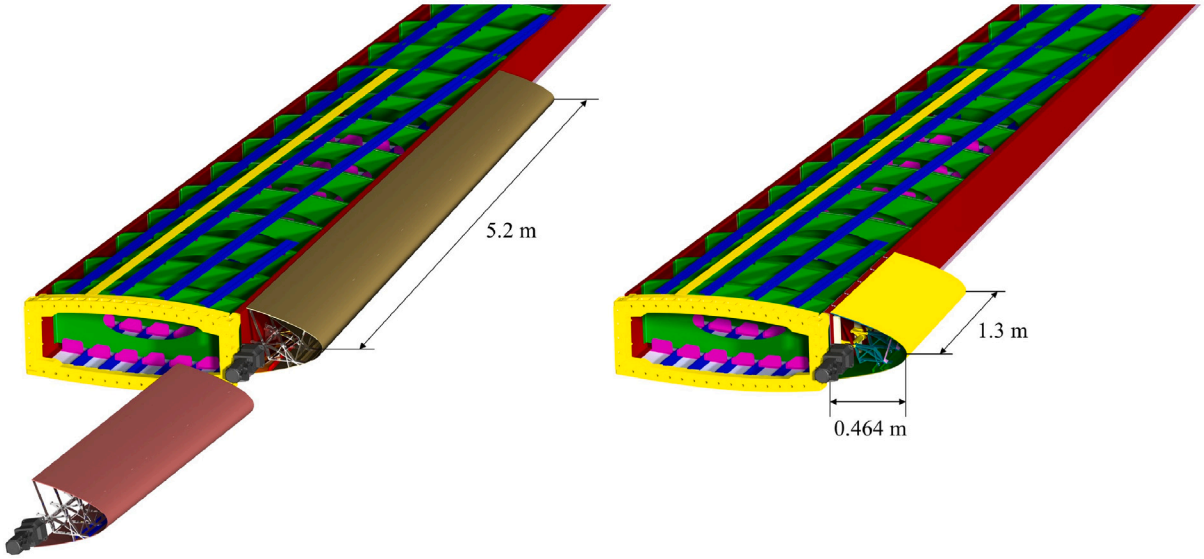

Fig. 5. Morphing droop nose installed on the wing-box: complete active device composed of its inboard and outboard regions (left) and experimental demonstrator (right).

2.4. Design of the complete device

The solutions obtained from the previously described design stages constituted the starting point for the design of the complete device. Although the sizing optimization was repeated for different sections along the span, the skin thickness, while varying along the chord, was kept uniform in the spanwise direction for manufacturing convenience. On the contrary, the ribs differ from each other in both in-plane thicknesses and size as the wing is tapered, and they are equally spaced by 260 mm. The rib sections are perpendicular to the front spar of the wing and the width of each rib is 40 mm. Four stringers were embedded into the skin to increase the spanwise stiffness, minimizing the anticlastic deformations, and to introduce the physical connections between the skin and the compliant ribs. As will be described in the next sections, the skin made of glass fiber was manufactured using two sequential curing stages. Finally, a dedicated kinematic chain was designed to transfer actuation from a single rotary motor to all compliant ribs, as shown in Fig. 4.

The complete device is shown in the left-hand side of Fig. 5. Based on this design, corresponding high-fidelity FEMs were generated to perform bird strike simulations [25] and virtual functionality tests aimed to check aeroelastic effects due to the interaction between wing-box and morphing droop nose [17]. These tests enabled to assess the impact of the wing-box deformability on the droop nose deployment capabilities. The results obtained from these further analyses led to small changes to the design up to the final solution which represents the starting point for the work presented in this article.

3. Full-scale prototype

After the design phase, an experimental prototype of the morphing droop nose is conceived to evaluate the morphing shape quality, and to validate the structural and mechanical concept at the full-scale level. The full-scale demonstrator is 1.3 m long in the spanwise direction which is less than the 5.2 m span of the active device in the outboard region of the wing, but is considered sufficient to study the 3D behavior of the device. The right-hand side of Fig. 5 shows the position and dimensions of the droop nose prototype installed on the outer wing-box, compared to the complete device shown on the left-hand side. The wing geometry is tapered, so the root and tip chords of the prototype are 464 mm and 438 mm long, respectively, while the front spar is 408 mm high at the root and 372 mm at the tip.

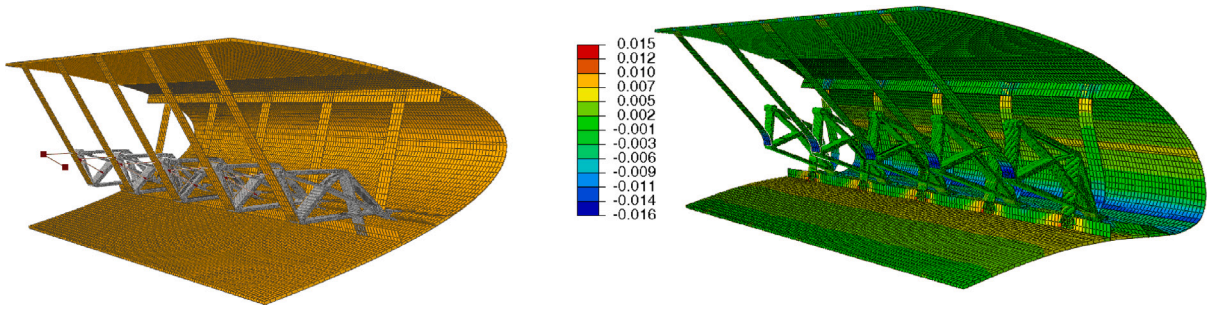

Fig. 6. Undeformed and deformed finite element model of the full-scale droop nose prototype, and maximum principal strain distribution.

3.1. Numerical modeling

A high-fidelity FEM of the prototype is realized in Abaqus™. The central body of the compliant ribs is modeled with solid elements, whereas skin, stringers and the parts of the ribs made of glass-fiber are modeled with shell elements. Tie constraints are used to connect the ribs to the stringers, and the different parts of the ribs to each other. Actuation is introduced by imposing a rotation at the points where the shaft axis intersects the rib planes. Rigid elements connected to each other by hinges transform the shaft rotation into the movements of the input points of the ribs, forming a kinematic chain like the one in Fig. 4. The connection between the kinematic chain and the compliant ribs is achieved through a continuum distributing coupling element, which links the displacement of the point belonging to the kinematic chain to the displacements of the nodes placed on the internal surface of a hole belonging to the ribs.

Nonlinear finite element analyses are performed to simulate the behavior of the device when actuated. An imposed displacement history is used to rotate the shaft from $0\,\mathrm{deg}$ to $80\,\mathrm{deg}$, while the aerodynamic loads, applied to the skin, increase from the pressure values obtained on the undeformed shape to the pressure values obtained on the target shape defined in Section 2.1. The aerodynamic loads correspond to the landing condition at $16\,\mathrm{deg}$ angle of attack (AoA). Since the final deformed shape approximates the target shape, the aerodynamic loads on the achieved deformed shape are considered accurate. The comparison between the initial and morphing configurations obtained from the finite element analysis is illustrated in Fig. 6. The same figure also highlights the distribution of the maximum principal strain which reaches peaks of 1.5% located at the connection points of the ribs with the stringers embedded into the skin, and at the point of maximum curvature variation of the skin. The corresponding Tsai-Hill failure index in the skin is depicted in Fig. 7, showing how the device at its maximum deflection does not achieve the composite material failure by a margin greater than 20%. The failure index reaches its maximum value at the same point where the skin reaches the maximum curvature variation.

In parallel with the strain analysis, the quality of the three-dimensional deformed shape is evaluated by comparing it with the target shape. The results are not discussed here because they will be presented in sections 5.1 and 6, after updating the FEM following the numerical/experimental correlation. However, it can be mentioned that the three-dimensional deformation is in good agreement with the target shape both considering and not considering aerodynamic loads applied to the skin. The deformed shape is therefore negligibly affected by the application of external loads. This confirms the results obtained by the MOGA described in Section 2.2 and that an optimum trade-off has been achieved between the conflicting requirements that characterize the morphing solution. The designed structure can deform to achieve the desired shape change and, at the same time, withstand the aerodynamic loads while being sufficiently insensitive to their variation.

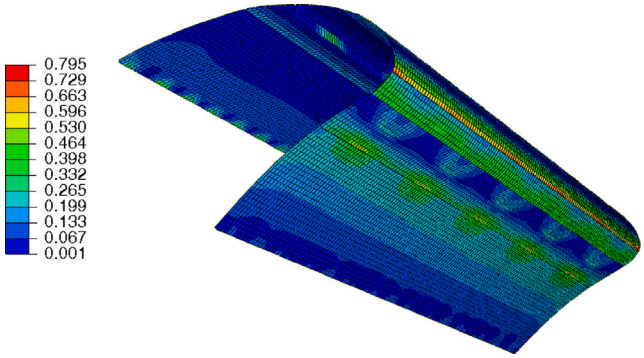

Fig. 7. Tsai-Hill failure index in the skin.

Table 1
Material properties of the glass-fiber fabric EE302S ER450 38%.

Parameter	Value
0° Tensile modulus	28.4 GPa
90° Tensile modulus	27.2 GPa
Poisson's ratio	0.16
In Plane Shear modulus	3.98 GPa
0° Tensile strength	687 MPa
0° Compressive strength	540 MPa
90° Tensile strength	580 MPa
90° Compressive strength	505 MPa
In Plane Shear strength	97.5 MPa
Elongation at failure	3.05%
Cured Ply Thickness	0.271 mm

3.2. Manufacturing

The manufacturing phase begins with the computer-aided design (CAD) of the prototype depicted in Fig. 8. The optimum thickness values of the parts made of glass-fiber, obtained from the sizing optimization described in Section 2.3, are approximated in this phase to obtain an integer number of plies, each characterized by a cured ply thickness equal to $0.271\,\mathrm{mm}$. A composite material made of S glass-fiber fabric and an epoxy resin is selected for the skin, the stringers, the parts of the ribs not made of aluminum, identified with a color other than green in the CAD model, and the spar to which the prototype connects. The material properties are reported in Table 1 and a lamination sequence of $[0, 90]_n$ has been selected for all these parts.

The skin is divided into sections of different thickness as depicted in Fig. 9 which also reports the number of plies needed for each section of the skin and for the stringers. The stringers are used to reinforce the skin in the spanwise direction and to introduce the physical connections between the skin and the compliant ribs. Each stringer is embedded into the skin using two sequential curing stages, so that the outer layer of stringers coincides with the inner layer of the skin. It should be noted that the optimization variables related to the skin cause a discretization

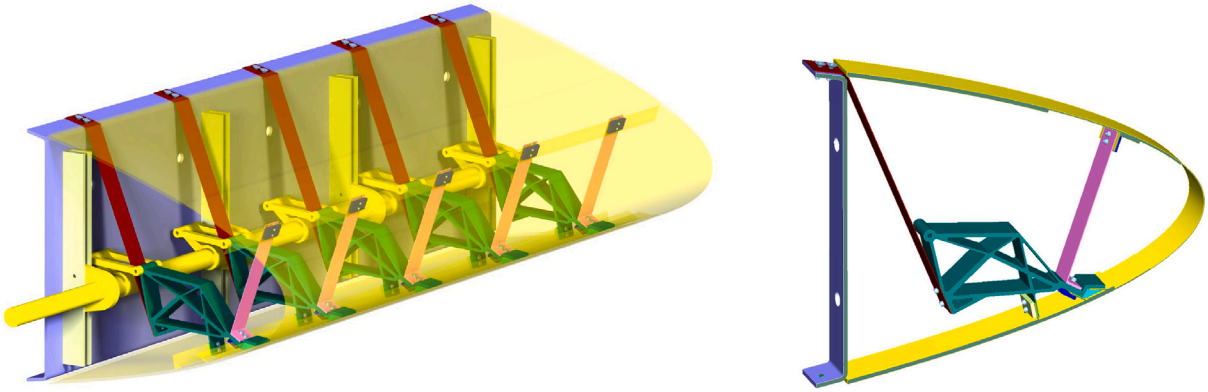

Fig. 8. CAD model of the full-scale prototype and details of connections between rib and skin.

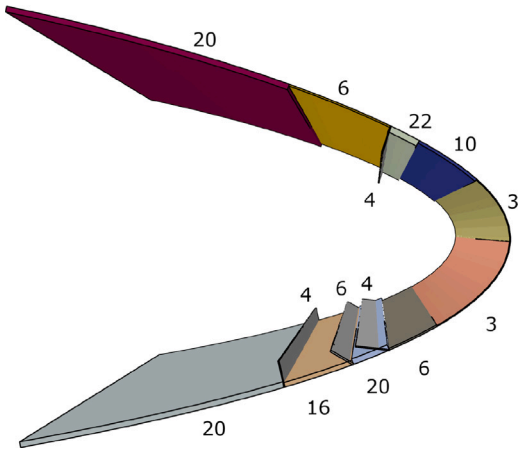

Fig. 9. Partition of constant thickness skin sections and number of plies for each skin region and for the stringers.

in constant-thickness sectors, determining an abrupt transition between two adjacent thicknesses in the above numerical models. This issue has been improved in the stacking phase by properly cutting the laminae to realize a gradual linear transition. This solution will prove helpful in obtaining smoother deformation of the external surface.

Dedicated mold and tools are realized for the curing process of the glass-fiber laminates, as depicted in the left-hand side of Fig. 10, which also shows the manufactured skin with embedded stringers and the front spar. A C-shape spar trunk, connected to the skin, represents the front spar of the wing-box that supports the droop nose device. It is also made of glass-fiber and is stiffened with honeycomb panels.

The material selected for the central body of the ribs is the high-strength 7075 aluminum alloy (Ergal), having an elastic modulus of 72 GPa. Water jet cutting technology is used to manufacture the aluminum part of the ribs and to cut cams and rods making up the kinematic chain.

Bolted joints are adopted to assemble the aluminum body of the ribs with their glass-fiber elements and to connect the ribs to the stringers, as shown in the right-hand side of Fig. 8. Particular attention is devoted to the actuation shaft supports that must sustain the reaction loads coming from the actuated ribs. The shaft is connected to the front spar via four supports housing the same number of ball bearings.

The fully-assembled prototype mounted on the test rig at the PoliMi's structural testing laboratory is shown in Fig. 11. The mass per unit span length of the morphing device is $9\,\mathrm{kg\,m^{-1}}$. Typical values of leading edge structures for regional aircraft are about $13\,\mathrm{kg\,m^{-1}}$ and $6.5\,\mathrm{kg\,m^{-1}}$ with and without slat, respectively [26].

4. Experimental testing

The main scope of the experimental test is the functionality assessment of the actuated device and its numerical/experimental correlation. This is essential to validate the proposed morphing concept and to demonstrate the effectiveness of the engineering solution at full-scale level using conventional aeronautical materials.

4.1. Experimental setup

The droop nose prototype has been mounted on the test rig using the front spar as an interface structure between the device and some modular blocks connected to a ground test platform. The front spar is connected to the blocks via 2 rows of five equally spaced bolted joints passing through the shear web, as depicted in Fig. 11. The skin is connected to the front spar via 20 equally spaced bolted screws placed along the upper spar cap and another 20 along the lower spar cap.

The instrumentation used for the test includes strain gauge sensors for force, torque and strain measurements, and a marker-based motion capture system for the identification of shape changes due to the morphing.

A full-bridge strain gauge configuration is used for measuring the actuation torque applied to the shaft via shear strains. A full-bridge configuration is used for measuring the axial force into the five rods that make up the kinematic chains used to transmit actuation in each compliant rib. A quarter-bridge configuration is used for measuring bending strains on the skin external surface. The first one can be seen in Fig. 11, the other two in Fig. 12. The adopted data acquisition system is the Micro-Measurements System 7000, while Vishay Micro-Measurements strain gauges are used, characterized by a grid resistance of $350\,\Omega$, a gauge factor equal to 2.15, and a maximum strain of 3%.

The actuation torque is directly measured on the shaft, but it can also be estimated from the axial forces acting on the connecting rods. The bending strain of the skin is measured on two sections located at 20% and 80% of the span, in the minimum thickness region where the greatest curvature change is expected. All these measurements will be used to perform the numerical/experimental correlation described in Section 5. Based on the outcome of this correlation, the FEM described in Section 3.1 will be updated and used for further numerical analyses that cannot be performed in the laboratory on the experimental demonstrator.

The identification of the external shape is based on a motion capture system provided by Qualisys. The system consists of eight 2 MP cameras. Once the system is calibrated, the cameras track the position of spherical markers installed on the object of interest, and the software computes the trajectories of the markers. The choice of the number and position of the markers installed on the outer surface of the skin is based on an approach aimed at finding the best compromise between the number of markers and the local error expected from an in-house

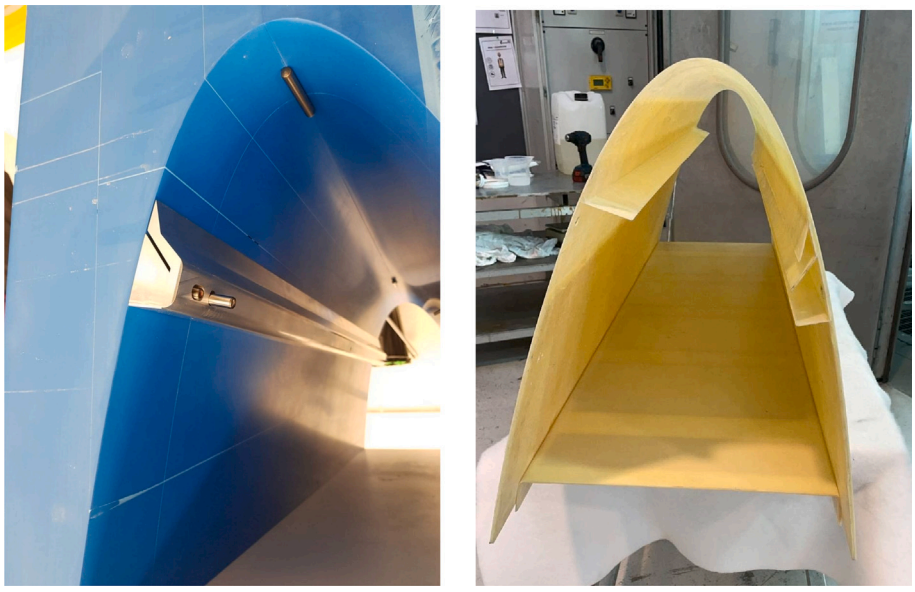

Fig. 10. The mold with tools and the glass-fiber skin, with embedded stringers, connected to the front spar.

Fig. 11. Full-scale prototype of the morphing droop nose.

procedure involving the FEM, which will be described below. At the end of this procedure, 155 markers have been used with a higher density in the leading edge region, where the greatest curvature change occurs. The arrangement of the cameras around the droop nose and the distribution of markers on the skin surface are depicted in Fig. 13. It should be noted that the black and white pattern painted on the surface was necessary for a different photogrammetry technique adopted in a preliminary test that was not used in this work.

A dedicated procedure has been developed to identify, in a post-processing phase, the shape of the entire outer surface of the skin. This procedure is based on a Radial Basis Function (RBF) technique and takes inspiration from the fluid–structure interaction techniques used in coupled aeroelastic simulations [27]. The interpolation of the markers' displacements, instead of the markers' positions, allows to overcome the issue related to the tracking of the markers' centroid, which has an offset from the surface in a normal direction that changes depending on the position of the markers. In the adopted procedure, the marker grid represents the coarser mesh whose displacements are measured by the motion capture system, thus defining the centers of the RBFs. The FEM grid represents the finer mesh describing the geometry where the displacements are interpolated. The Wendland C^2 compactly supported function [28] is used during this work and the RBF scheme interpolates in three-dimensional space. This procedure has been applied to the undeformed prototype to establish the number and position of markers, as mentioned above, and used to evaluate the quality of its deformation in Sections 5.1 and 6.1.

4.2. Functionality test

The experimental test is conducted by applying a torque to the shaft through a lever actuated by a motorized hoist positioned above the prototype. The hoist applies an upward force to the lever to reach a certain shaft rotation, measured with an inclinometer, and the device is held in that position for a few seconds before further increasing the deflection level. This loading cycle is repeated until the desired maximum deflection is achieved. Strain gauge sensors are continuously acquiring data during the device deployment, while cameras track the motion of the markers.

The deflection is increased by monitoring the strain values measured on the skin, using the limit considered in Section 2.1 as a conservative reference. The shaft rotation is stopped at 65 deg, corresponding to 12.5 deg equivalent rotation, when a 1.14% maximum strain is measured by the strain gauge located at 80% of the span. The glass-fiber material used to build the skin would allow to go beyond this deflection, but the test was interrupted so as not to compromise the structural integrity of the prototype, also considering the lamination uncertainties. The strain values acquired by the two strain gauges during the entire load cycle are shown in Fig. 14, together with the corresponding values obtained from the FEM. The experimentally measured strain values are 8% higher than the numerical values. Looking at the experimental curves, a 1% maximum strain occurs at about 60 deg shaft rotation, corresponding to an equivalent rotation of 11.3 deg.

The comparison between the undeformed shape and the deformed shape obtained at 65 deg shaft rotation is represented in Fig. 15. The behavior of the internal structure matches the FEM prediction, previously shown in Fig. 6. The complete deformed configuration of the prototype is also depicted in Fig. 16.

5. Experimental validation

The data acquired during the experimental test are compared with the numerical results and used to perform a numerical/experimental

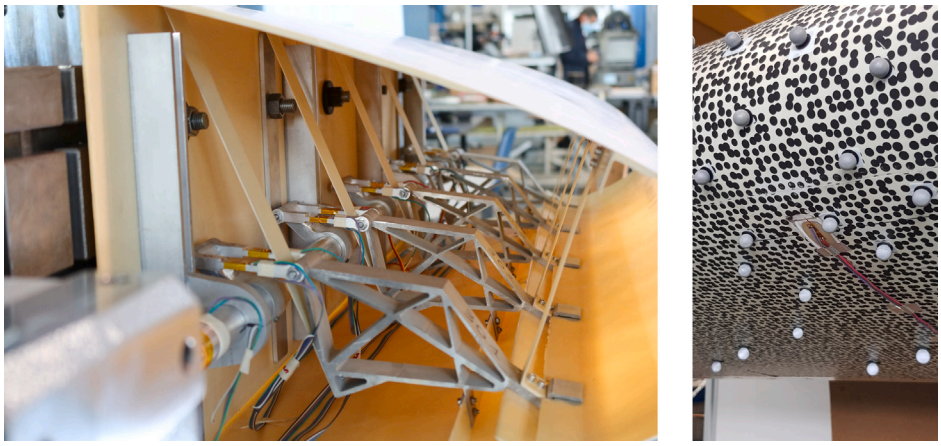

Fig. 12. Strain gauges installed on the prototype for measuring the axial strain of the rods (left) and the bending strains on the skin (right).

Fig. 13. Motion capture system setup: position of cameras and distribution of markers.

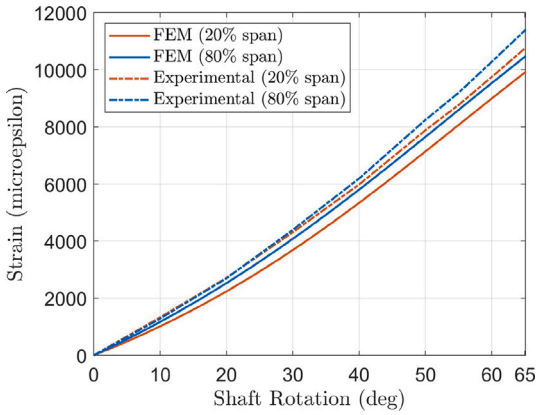

Fig. 14. Maximum strains in the skin as functions of the shaft rotation: comparison between numerical and experimental results.

correlation, providing an updated FEM. The comparison is based on both strain gauge measurements and the experimental shape identification described in the previous section.

The numerical/experimental correlation begins with the comparison between the numerical and the experimental actuation torque which are represented in Fig. 17. The experimental torque is derived from the axial forces measured in the rods, to ensure that the updating process is not affected by the friction due to the coupling between the shaft and the supports. The numerical torque is computed as the sum of the torque contributions of each rib, obtained as the product of the axial forces and the local distance between the rods and the shaft axis. The dependence of these distances on the shaft rotation is evaluated by the numerical simulation. Thanks to the adoption of ball bearings, the friction computed as the difference between the torque derived from the axial forces and the torque measured directly on the shaft is negligible. Indeed, the device tries to spring back towards the initial configuration as soon as the applied torque is removed. This is a consequence of the strain energy stored in the device and highlights the elastic behavior of the device. For this reason, the device should be equipped with a brake to keep the desired position without power consumption.

Analyzing Fig. 17, the numerical torque is 58% higher than the experimental torque at 65 deg shaft rotation. A similar comparison is carried out between the numerical and experimental strain energies which are depicted in Fig. 18. The experimental strain energy is calculated as the work done by the actuation torque to rotate the shaft, thus computing the integral of the curves in Fig. 17. This calculation assumes that friction in the compliant device as well as inertial contributions due to the slow rotation of the shaft are negligible. The numerical strain energy is 44% higher than the experimental strain energy at 65 deg.

The difference between experimental and numerical results is investigated by evaluating the different strain energy contributions in the numerical model. The contribution of the skin represents 91% of the total strain energy. Therefore, the FEM updating is performed by changing the elastic modulus assigned to the glass-fiber fabric material, with the aim of minimizing the discrepancy between the numerical and experimental strain energy curves. It is assumed that

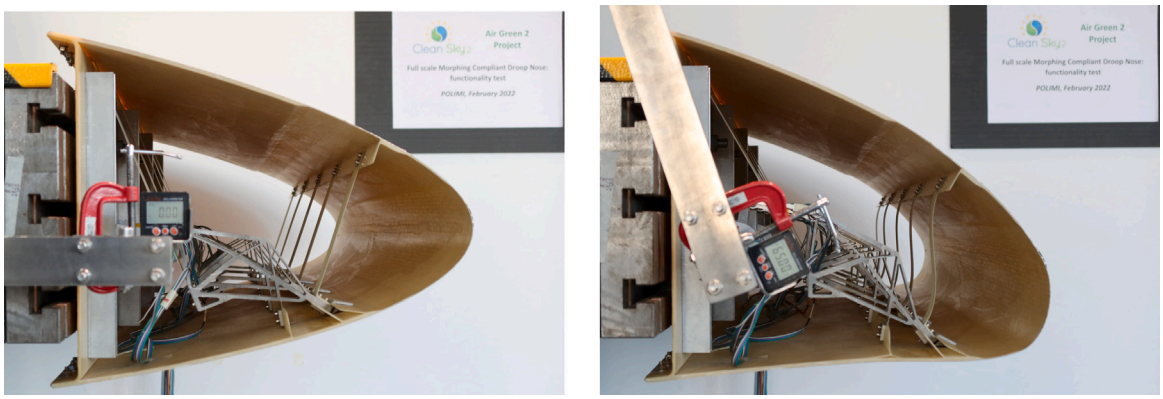

Fig. 15. Comparison between the undeformed and the deformed prototype.

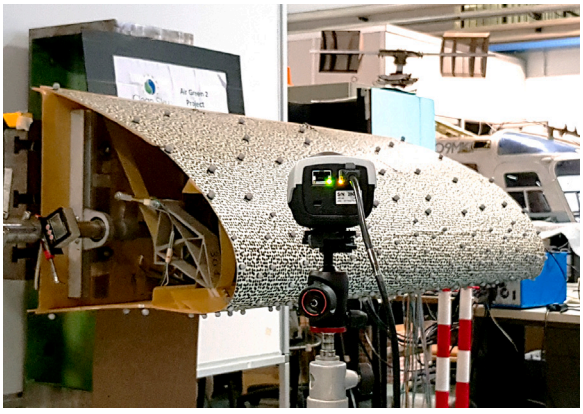

Fig. 16. Deformed shape of the full-scale prototype at 65 deg shaft rotation.

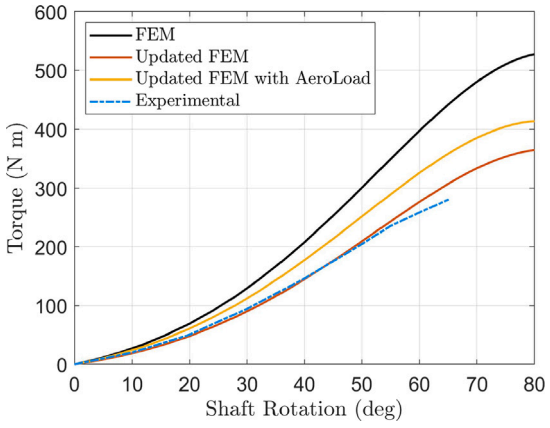

Fig. 17. Actuation torque comparisons as functions of the shaft rotation.

the actual mechanical properties of the material can be lower than those reported in the data sheet due to manufacturing issues related to the lamination process, such as an incorrect orientation of the fibers and some difficulties encountered in the deposition of the fabric layers in the high curvature regions of the mold. A 31% reduction in the elastic modulus is carried out to make the updated FEM model capable of fitting the experimental strain energy trend, as shown in Fig. 18. The corresponding actuation torque is also improved while still exhibiting some differences that are shown in Fig. 17. Comparison of skin deformation values is not reported because they are not affected by the updating process.

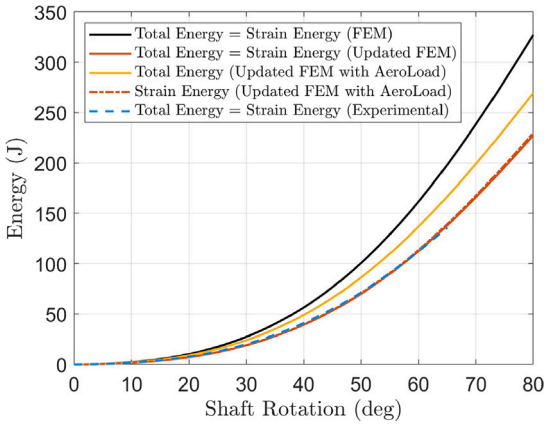

Fig. 18. Actuation energy comparisons as functions of the shaft rotation.

5.1. Final updating for shape quality improvement

The comparison between the identified experimental shape and the deformation of the updated FEM, both obtained at 65 deg shaft rotation, shows that they are almost overlapping. A numerical quantification of the geometric error is performed using the RBF-based procedure described in Section 4.1 and the result is reported in the left-hand side of Fig. 19. The highest error values of 7.6 mm are reported on the upper surface of the droop nose, whereas the root mean square error computed over the entire skin surface is 4.2 mm. While the shape comparison is globally satisfying, the largest discrepancy is concentrated on the upper skin. The FEM deformation exhibits a kind of beveled corner at the upper stringer's location, whereas the experimental deformation is smooth. This can be due to the abrupt thickness change that characterizes the FEM in that skin region. The maximum local error corresponds to 27% of the local displacement and could be improved with a model updating. Therefore, the FEM is updated a second time by including gradual thickness transitions between adjacent sectors of the skin, similarly to what was done for the experimental prototype. Thanks to this local modification the numerical deformation becomes smoother and the shape correlation improves, as depicted in Fig. 19 which compares the error distribution before and after the second updating process. This modification does not affect the energetic considerations outlined above. The discrepancy between the experimental shape and the deformation of the final updated FEM is now characterized by a maximum local error of 5.9 mm, whereas the root mean square error computed over the entire skin surface drops to 3.6 mm. The maximum local error decreases to 21% of the local displacement. Despite the reduction achieved, the error still seems large because the local shape variation of the device is small in this region.

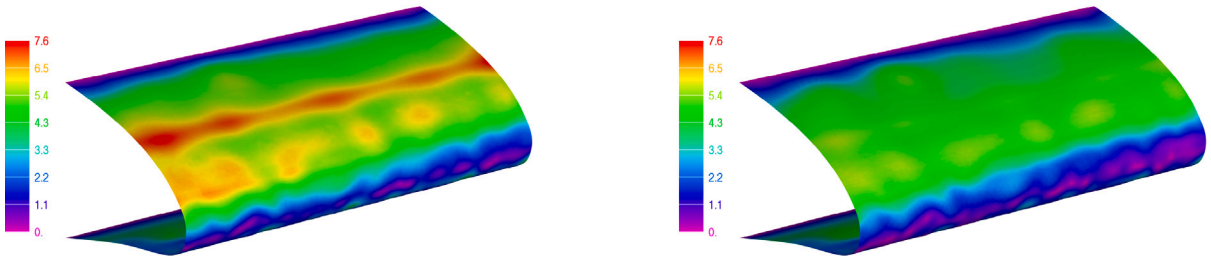

Fig. 19. Shape comparison at 65 deg shaft rotation: local error (mm) between the experimental deformation and the numerical deformation of the updated FEM before (left) and after (right) including gradual thickness transitions into the skin.

However, this region is narrow and the local error is small compared to the maximum shape changes of the complete device. Indeed, the residual error has no effect on the overall aerodynamic performance, as will be seen in the following.

6. Performance assessment

Once the updated FEM is available and able to reproduce the behavior of the experimental prototype, it can be used to thoroughly investigate the morphing device. Performance assessment includes two additional virtual tests: a functionality test to evaluate the capability of the device to achieve the target shape while remaining insensitive to variations in external aerodynamic loads; a series of aeroelastic analyses, based on CFD simulations, aimed at verifying that the aerodynamic performance of the deformed device corresponds to that of the target shape resulting from the shape optimization described in Section 2.1.

6.1. Validation of structural performances

The updated FEM model is first used to simulate the structural behavior of the device subjected to the aerodynamic loads, in the flight conditions relevant for the use of the device. In particular, we are interested in evaluating how the application of the aerodynamic loads affects the device in terms of deformation, shape change, and energy. Thanks to the multi-objective approach adopted during the design of compliant structures, the deformation due to the external loads should be limited. The verification is performed by simulating the structural solution of the updated model under pressure loads in landing condition for two cases, namely 10 deg and 16 deg angles of attack. The local difference between the two deformed shapes is depicted in Fig. 20 and gives a root mean square deviation of 1.3 mm. This difference represents the sensitivity of the deformed shape to the application of aerodynamic loads. The greatest discrepancy is found on the upper skin which is the most loaded region characterized by a small thickness of the skin. Indeed, here there is a peak of negative pressure, as shown in Fig. 3, and the small thickness is needed to realize the large curvature variation on the upper skin [24]. However, the maximum difference of 3.9 mm corresponds to less than 1% of the device chord length, confirming the ability of the designed compliant structure to make negligible the wing shape deformation at different loading conditions.

The deformations of the updated model are then compared with the target shape, considering both 10 deg and 16 deg angles of attack. The results are shown in Fig. 21. The local difference between the deformed and target shapes assumes higher values than the local difference shown in Fig. 20. This means that the sensitivity of the morphing deformation to the variation of aerodynamic loads is much lower than the error compared to the target shape. However, as it will be shown in Section 6.2, it does not make an appreciable difference in the aerodynamic performances.

Finally, the effect of the external loads on the skin strain is investigated, showing that the maximum strain increases by 3% compared to the unloaded case. Therefore, at the local level, the presence of the aerodynamic loads has a minimum effect in terms of shape and

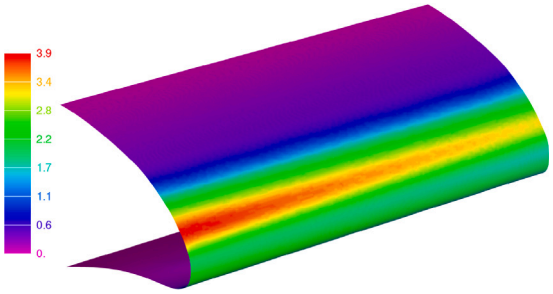

Fig. 20. Local difference (mm) between the numerical deformation computed considering the aerodynamic loads at 10 deg and 16 deg angles of attack.

strains. The situation is different from the energy point of view. The total energy of the loaded device reported in Fig. 18 is the sum of two contributions: the former is the strain energy associated with the shape change due to the morphing, the latter is the work associated with the external aerodynamic loads. The total energy of the loaded device is higher than the energy of the device subject only to the actuation torque. At the maximum shaft rotation, the actuation energy required applying aerodynamic loads is 19% higher than in the case without loads and the corresponding actuation torque is 13% higher. Moreover, contributions to the total energy can be divided into the 84% needed to deform the structure and the 16% needed to withstand the external loads. Therefore, for this leading edge device the dominant contribution to the required actuation energy is associated with the morphing process. The effect of the external aerodynamics loads is lower, although not negligible from an energy point of view.

6.2. Validation of aerodynamic performances

The developed prototype is not intended for wind tunnel testing, therefore the validation of the aerodynamic performance associated with the obtained deformed shape is conducted numerically. The results of the nonlinear finite element analyses are used to produce a CFD model covering the same portion of the wing as the experimental demonstrator. The CFD simulations are performed using the SU2 open-source code [29] and are based on Reynolds-averaged Navier-Stokes (RANS) equations, selecting the Menter's Shear Stress Transport (SST) turbulence model.

The ability of the device to be insensitive to the variation of aerodynamic loads was exploited to perform a linear static aeroelastic analysis without simulating the entire actuation history. After the updated finite element model is actuated to achieve the 16 deg maximum deflection, the aerodynamic loads coming from the CFD simulations are applied to the skin and updated iteratively along with the CFD mesh deformation. Since the aerodynamic loads have minimum effects on the deformation of the finite element model, the linear static aeroelastic analysis converges in two iterations.

The CFD mesh is depicted in Fig. 22 in its undeformed configuration. It is characterized by approximately 6 million vertices and,

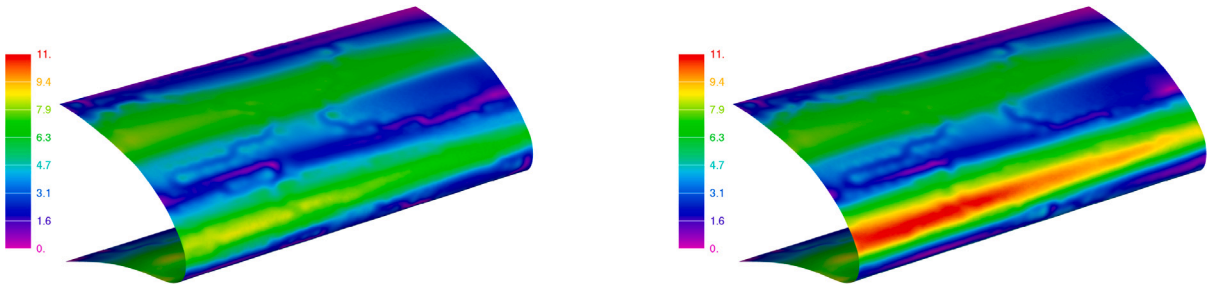

Fig. 21. Local difference (mm) between the target shape and the numerical deformation at 10 deg (left) and 16 deg (right) angles of attack.

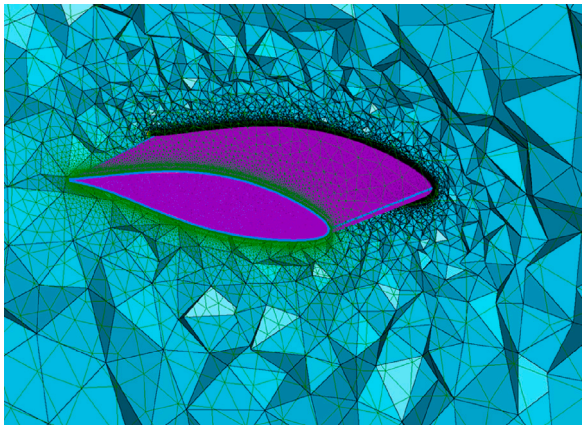

Fig. 22. CFD mesh corresponding to the undeformed wing portion.

although barely visible, finer structured mesh cells are used for the boundary layer. The aerodynamic model is representative of a wind tunnel experiment in which the device covers the entire span of the test section. Therefore, two walls are placed at the root and tip of the wing with no penetration boundary conditions. No-slip boundary condition is adopted at the wing surface, whereas the far field boundary condition determines the flow variables using Riemann invariants. Due to the limited spanwise extension of the aerodynamic model, the aim of the aerodynamic evaluation is not the validation of the aircraft performance, but rather the assessment of the achieved deformed shape compared with the target and the undeformed shapes.

The analyses are repeated for different angles of attack, from 0 deg to 21 deg, in landing flight condition at sea level (Mach = 0.197). Three different shapes are analyzed, namely the undeformed shape, the target shape, and the deformed shape achieved by the updated model. The lift coefficient as a function of AoA and the polar curve are compared in Fig. 23. Moreover, the undeformed and deformed shape are compared in Fig. 24 for 20 deg AoA, in terms of streamlines and momentum along the wind direction.

The aerodynamic results for the deformed shape show negligible differences compared to the target shape despite the geometrical discrepancy highlighted in Fig. 21. Therefore, they demonstrate that the aerodynamic performance which the designed device can provide corresponds to those of the target shape, even showing less aerodynamic drag in the conditions around stall. Moreover, the comparison between the results obtained using the undeformed and the deformed shape confirms that the droop nose device is effective in delaying the stall onset, while the undeformed configuration is characterized by a wider separation region that penalizes the lift production at high incidence.

A final note concerns the values of the aerodynamic coefficients shown in Fig. 23. They do not refer to the complete aircraft, being valid only for the designed prototype which has a limited spanwise extension. Therefore, the obtained results cannot be compared with the aircraft performance presented in [24], but they are meaningful for the assessment of the designed device with respect to the target shape, concluding the validation phase.

7. Conclusions

This paper has described the experimental validation of a morphing droop nose design. The device, designed to be installed on the innovative wing of a regional aircraft, has been conceived to provide high-lift capabilities in take-off and landing conditions, together with a smooth and gap-less skin surface. A multi-level and multi-disciplinary optimization procedure has been adopted to design and validate the concept. Starting from the performance augmentation requirements, an optimal target shape has been determined and used to drive the design of the compliant structure in the initial phase of the project. Then, the work concentrated on the design and the experimental validation of a full-scale prototype of the morphing droop nose device. A detailed finite element model of the complete prototype has been realized and the numerical results have assessed the structural feasibility and the quality of the achieved morphing shape. Manufacturing and assembly phases have proven to be effective, and the adopted processes seem promising for the industrialization of the designed device. The experimental test of the full-scale prototype has assessed the functionality of the device and demonstrated the effectiveness of the engineering solution, showing an elasto-mechanical behavior that is consistent with the numerical simulation. A motion capture technique has proven to be a viable solution to identify the experimental external shape which has been compared with the results of numerical simulations. A numerical/experimental correlation has been performed aimed at minimizing the strain energy discrepancy between experimental results and numerical simulations. An updated numerical model, matching the experimental strain energy, has been obtained after two validation loops. The updated model has been used to assess the stiffness of the device under external loads, proving that the droop nose deflection and the quality of the deformation does not depend on variations in flight conditions. Moreover, the

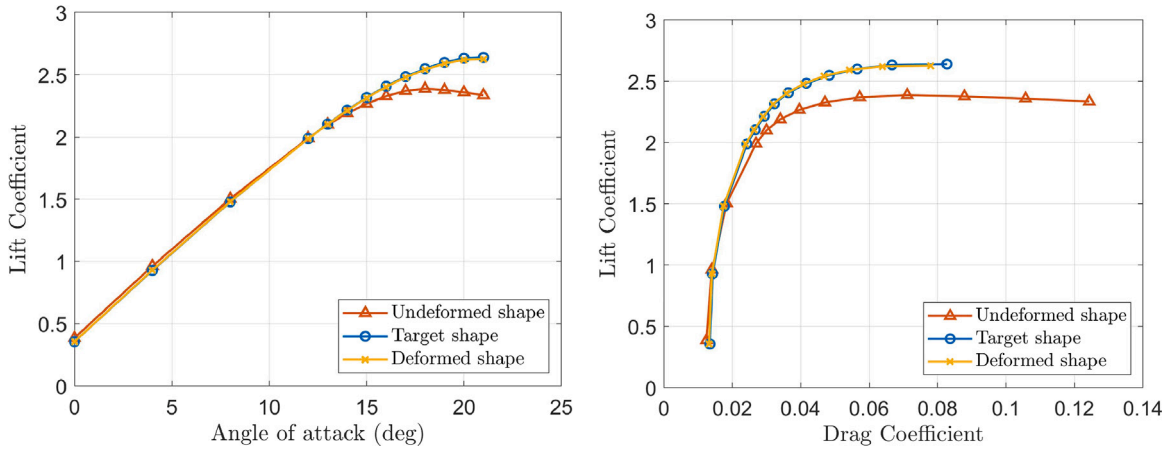

Fig. 23. Comparison between CFD results of undeformed shape, optimal target shape and updated FEM deformed shape: lift coefficient vs AoA (left) and polar curves (right) in landing flight condition at sea level.

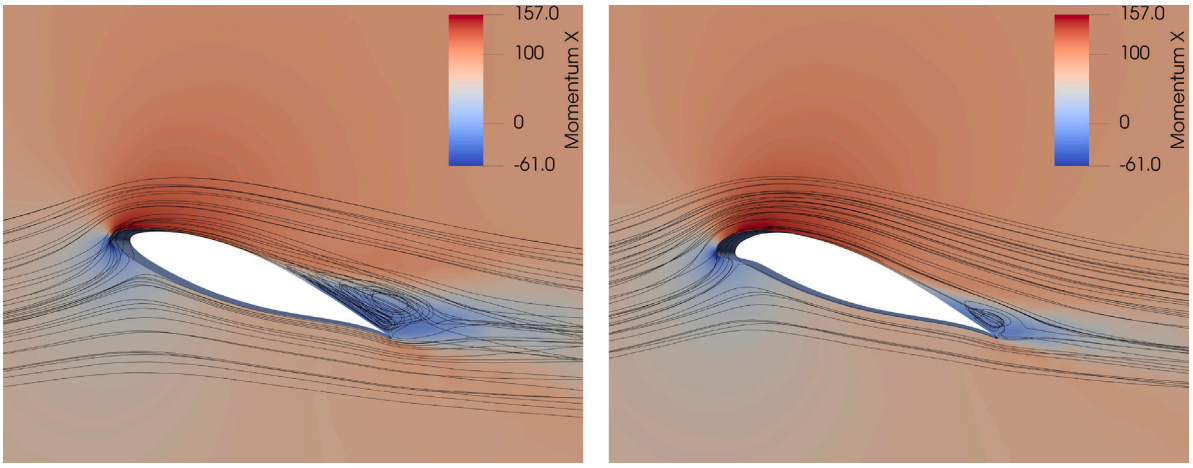

Fig. 24. CFD results in terms of momentum ($\mathrm{kg\,m^{-2}\,s^{-1}}$) along the wind direction and streamlines, at 20 deg AoA: comparison between undeformed shape (left) and updated FEM deformation (right) in landing flight condition at sea level.

total energy stored in the droop nose has been numerically investigated, showing that the strain energy due to the morphing process prevails over the work done to counteract the aerodynamic loads. Finally, high-fidelity calculations demonstrated that the external shape change achieved by the designed device guarantees the same aerodynamic performances as the optimal target shape defined at the beginning of the design.

CRediT authorship contribution statement

Alessandro De Gaspari: Writing – original draft, Validation, Supervision, Software, Resources, Methodology, Investigation, Conceptualization, Writing – review & editing, Visualization. **Vittorio Cavalieri:** Writing – original draft, Software, Formal analysis, Investigation, Data curation, Writing – review & editing, Visualization. **Sergio Ricci:** Project administration, Funding acquisition.

Declaration of competing interest

The authors declare that they have no known competing financial interests or personal relationships that could have appeared to influence the work reported in this paper.

Data availability

Data will be made available on request.

Acknowledgments

The AirGreen2 Project has received funding from the Clean Sky 2 Joint Undertaking, under the European's Union Horizon 2020 research and innovation Programme, under grant agreement No. 807089. A special thanks to Nicola Fonzi for his support in the realization of the CFD mesh used for the final performance assessment.

References

[1] Zhang J, Bisagni C. Buckling-driven mechanisms for twisting control in adaptive composite wings. Aerosp Sci Technol 2021;118:1–11. http://dx.doi.org/10.1016/j.ast.2021.107006.

[2] Heo H, Ju J, Kim D-M. Compliant cellular structures: Application to a passive morphing airfoil. Compos Struct 2013;106:560–9. http://dx.doi.org/10.1016/j.compstruct.2013.07.013.

[3] Zhi Q, Li D, Sun H, Zhu W. Adjustment of multi-directional elastic properties of chiral metamaterial via a 3D printing-based soft-hard bi-material strategy. Compos Struct 2023;307:116646. http://dx.doi.org/10.1016/j.compstruct.2022.116646.

[4] Lemos DM, Marques FD, Ferreira AJ. A review on bistable composite laminates for aerospace applications. Compos Struct 2024;329:117756. http://dx.doi.org/10.1016/j.compstruct.2023.117756.

[5] Hoa S, Abdali M, Jasmin A, Radeschi D, Prats V, Faour H, et al. Development of a new flexible wing concept for unmanned aerial vehicle using corrugated core made by 4D printing of composites. Compos Struct 2022;290:115444. http://dx.doi.org/10.1016/j.compstruct.2022.115444.

[6] Dayyani I, Shaw A, Flores ES, Friswell M. The mechanics of composite corrugated structures: A review with applications in morphing aircraft. Compos Struct 2015;133:358–80. http://dx.doi.org/10.1016/j.compstruct.2015.07.099.
[7] Woods BKS, Friswell MI. Preliminary investigation of a fishbone active camber concept. In: ASME 2012 conference on smart materials, adaptive structures and intelligent systems. vol. 2, Stone Mountain, Georgia, USA; 2012, p. 555–63. http://dx.doi.org/10.1115/SMASIS2012-8058, Mechanics and Behavior of Active Materials; Integrated System Design and Implementation; Bio-Inspired Materials and Systems; Energy Harvesting.
[8] Smith JW, Lock WP, Payne GA. Variable-camber systems integration and operational performance of the AFTI/F-111 mission adaptive wing. Tech. Rep., NASA Technical Report Server; 1992, URL https://ntrs.nasa.gov/archive/nasa/casi.ntrs.nasa.gov/19920012951.pdf.
[9] Vasista S, Nolte F, Monner HP, Horst P, Burnazzi M. Three-dimensional design of a large-displacement morphing wing droop nose device. J Intell Mater Syst Struct 2018;29(16):3222–41. http://dx.doi.org/10.1177/1045389X18770863.
[10] Rudenko A, Hannig A, Monner HP, Horst P. Extremely deformable morphing leading edge: Optimization, design and structural testing. J Intell Mater Syst Struct 2018;29(5):764–73. http://dx.doi.org/10.1177/1045389X17721036.
[11] Kintscher M, Monner HP, Heintze O. Experimental testing of a smart leading edge high lift device for commercial transportation aircrafts. In: 27th international congress of the aeronautical sciences. ICAS, Nice, France; 2010, p. 1–7.
[12] Thuwis GAA, Abdalla MM, Gürdal Z. Optimization of a variable-stiffness skin for morphing high-lift devices. Smart Mater Struct 2010;19(12):1–10. http://dx.doi.org/10.1088/0964-1726/19/12/124010.
[13] Kirn J, Storm S. Kinematic solution for a highly adaptive droop nose. In: 25th international conference on adaptive structures and technologies. ICAST, The Hague, The Netherlands; 2014, p. 1–11.
[14] Sodja J, Martinez MJ, Simpson JC, Breuker RD. Experimental evaluation of a morphing leading edge concept. J Intell Mater Syst Struct 2019;30(18 – 19):2953–69. http://dx.doi.org/10.1177/1045389X19862369.
[15] Han M-W, Rodrigue H, Kim H-I, Song S-H, Ahn S-H. Shape memory alloy/glass fiber woven composite for soft morphing winglets of unmanned aerial vehicles. Compos Struct 2016;140:202–12. http://dx.doi.org/10.1016/j.compstruct.2015.12.051.
[16] Lu K-J, Kota S. An effective method of synthesizing compliant adaptive structures using load path representation. J Intell Mater Syst Struct 2005;16:307–17.
[17] De Gaspari A. Multiobjective optimization for the aero-structural design of adaptive compliant wing devices. Appl Sci 2020;10(18):30. http://dx.doi.org/10.3390/app10186380.
[18] Dimino I, Moens F, Pecora R, De Gaspari A, Ricci S, Ameduri S, et al. Morphing wing technologies within the airgreen 2 project. In: 2022 AIAA scitech forum. San Diego, CA, USA & Virtual; 2022, p. 1–12. http://dx.doi.org/10.2514/6.2022-0718.
[19] Cavalieri V, De Gaspari A, Ricci S. Optimization of compliant adaptive structures in the design of a morphing droop nose. Smart Mater Struct 2020;29(7):22. http://dx.doi.org/10.1088/1361-665X/ab8902.
[20] De Gaspari A, Ricci S. Knowledge-based shape optimization of morphing wing for more efficient aircraft. Int J Aerosp Eng 2015;325724:1–19. http://dx.doi.org/10.1155/2015/325724.
[21] Rea F, Amoroso F, Pecora R, Noviello MC, Arena M. Structural design of a multifunctional morphing fowler flap for a twin-prop regional aircraft. In: ASME 2018 conference on smart materials, adaptive structures and intelligent systems. San Antonio, Texas, USA; 2018, p. 1–9. http://dx.doi.org/10.1115/SMASIS2018-7937, Development and Characterization of Multifunctional Materials; Modeling, Simulation, and Control of Adaptive Systems; Integrated System Design and Implementation.
[22] Cambier L, Heib S, Plot S. The onera elsa CFD software: input from research and feedback from industry. Mech Ind 2013;14(3):159–74. http://dx.doi.org/10.1051/meca/2013056.
[23] De Gaspari A, Ricci S. A two-level approach for the optimal design of morphing wings based on compliant structures. J Intell Mater Syst Struct 2011;22(10)):1091–1111. http://dx.doi.org/10.1177/1045389X11409081.
[24] De Gaspari A, Moens F. Aerodynamic shape design and validation of an advanced high-lift device for a regional aircraft with morphing droop nose. Int J Aerosp Eng 2019;7982168:1–22. http://dx.doi.org/10.1155/2019/7982168.
[25] De Gaspari A, Cavalieri V, Ricci S. Advanced design of a full-scale active morphing droop nose. Int J Aerosp Eng 2020;1086518:1–19. http://dx.doi.org/10.1155/2020/1086518.
[26] De Gaspari A, Ricci S, Antunes A, Odaguil F, Lima G. Chapter 6: Expected performances. In: Morphing wing technologies – large commercial aircraft and civil helicopters. Butterworth–Heinemann, Elsevier; 2018, p. 175–203. http://dx.doi.org/10.1016/B978-0-08-100964-2.00006-X.
[27] Beckert A, Wendland H. Multivariate interpolation for fluid–structure-Interaction problems using radial basis functions. Aerosp Sci Technol 2001;5(2):125–34. http://dx.doi.org/10.1016/S1270-9638(00)01087-7.
[28] Wendland H. Piecewise polynomial, positive definite and compactly supported radial functions of minimal degree. Adv Comput Math 1995;4:389–96.
[29] Palacios F, Alonso J, Duraisamy K, Colonno M, Hicken J, Aranake A, et al. Stanford University Unstructured (SU^2): An open-source integrated computational environment for multi-physics simulation and design. In: 51st AIAA aerospace sciences meeting including the new horizons forum and aerospace exposition. Grapevine, Texas; 2013, p. 1–60. http://dx.doi.org/10.2514/6.2013-287.